

Fully integrated hybrid silicon two dimensional beam scanner

J. C. Hulme,* J. K. Doyle, M. J. R. Heck, J. D. Peters, M. L. Davenport,
J. T. Bovington, L. A. Coldren, and J. E. Bowers

Electrical & Computer Engineering Department University of California Santa Barbara, California 93106, USA
*jaredhulme@ece.ucsb.edu

Abstract: In this work we present the first fully-integrated free-space beam-steering chip using the hybrid silicon platform. The photonic integrated circuit (PIC) consists of 164 optical components including lasers, amplifiers, photodiodes, phase tuners, grating couplers, splitters, and a photonic crystal lens. The PIC exhibited steering over $23^\circ \times 3.6^\circ$ with beam widths of $1^\circ \times 0.6^\circ$.

©2015 Optical Society of America

OCIS codes: (130.0130) Integrated optics; (060.2605) Free-space optical communication; (250.5300) Photonic integrated circuits; (280.3640) LIDAR.

References and links

1. M. J. R. Heck, J. F. Bauters, M. L. Davenport, J. K. Doyle, S. Jain, G. Kurczveil, S. Srinivasan, Y. Tang, and J. E. Bowers, "Hybrid silicon photonic integrated circuit technology," *IEEE J. Sel. Top. Quantum Electron.* **19**, 6100117 (2013).
 2. K. Van Acoleyen, W. Bogaerts, J. Jägerová, N. Le Thomas, R. Houdré, and R. Baets, "Off-chip beam steering with a one-dimensional optical phased array on silicon-on-insulator," *Opt. Lett.* **34**(9), 1477–1479 (2009).
 3. K. Van Acoleyen, H. Rogier, and R. Baets, "Two-dimensional optical phased array antenna on silicon-on-insulator," *Opt. Express* **18**(13), 13655–13660 (2010).
 4. D. Kwong, A. Hosseini, Y. Zhang, and R. T. Chen, " 1×12 Unequally spaced waveguide array for actively tuned optical phased array on a silicon nanomembrane," *Appl. Phys. Lett.* **99**(5), 051104 (2011).
 5. J. K. Doyle, M. J. Heck, J. T. Bovington, J. D. Peters, L. A. Coldren, and J. E. Bowers, "Two-dimensional free-space beam steering with an optical phased array on silicon-on-insulator," *Opt. Express* **19**(22), 21595–21604 (2011).
 6. J. Sun, E. Timurdogan, A. Yaacobi, E. S. Hosseini, and M. R. Watts, "Large-scale nanophotonic phased array," *Nature* **493**(7431), 195–199 (2013).
 7. J. K. Doyle, M. J. R. Heck, J. T. Bovington, J. D. Peters, M. L. Davenport, L. A. Coldren, and J. E. Bowers, "Hybrid III/V silicon photonic source with integrated 1D free-space beam steering," *Opt. Lett.* **37**(20), 4257–4259 (2012).
 8. J. K. Doyle, M. J. R. Heck, J. T. Bovington, J. D. Peters, M. L. Davenport, and J. E. Bowers, "Hybrid III-V silicon photonic steerable laser," *IEEE Photonics Conference*, Sept 23–27, 2012.
 9. J. K. Doyle, M. J. R. Heck, J. T. Bovington, J. D. Peters, M. L. Davenport, L. A. Coldren, J. E. Bowers, "Hybrid silicon free-space source with integrated beam steering," *Proc. SPIE 8629, Silicon Photonics VIII*, (2013).
 10. A. Yaacobi, J. Sun, M. Moresco, G. Leake, D. Coolbaugh, and M. R. Watts, "Integrated phased array for wide-angle beam steering," *Opt. Lett.* **39**(15), 4575–4578 (2014).
 11. C. Zhang, S. Srinivasan, Y. Tang, M. J. R. Heck, M. L. Davenport, and J. E. Bowers, "Low threshold and high speed short cavity distributed feedback hybrid silicon lasers," *Opt. Express* **22**(9), 10202–10209 (2014).
 12. J. C. Hulme, J. K. Doyle, and J. E. Bowers, "Widely tunable Vernier ring laser on hybrid silicon," *Opt. Express* **21**(17), 19718–19722 (2013).
 13. J. K. Doyle, M. J. R. Heck, J. T. Bovington, J. D. Peters, and J. E. Bowers, "Free-space beam steering using silicon waveguide surface gratings," *IEEE Photonics Conference*, 547–548 (2011).
 14. H. Park, Y.-H. Kuo, A. W. Fang, R. Jones, O. Cohen, M. J. Paniccia, and J. E. Bowers, "A Hybrid AlGaInAs-Silicon Evanescent Amplifier," *IEEE Photon. Technol. Lett.* **19**(4), 230–232 (2007).
 15. A. W. Fang, M. N. Sysak, B. R. Koch, R. Jones, E. Lively, Y.-H. Kuo, D. Liang, O. Rada, and J. E. Bowers, "Single-Wavelength Silicon Evanescent Lasers," *IEEE J. Sel. Top. Quantum Electron.* **15**(3), 535–544 (2009).
 16. J. K. Doyle, P. E. Jessop, and A. P. Knights, "Silicon photonic dynamic optical channel leveler with external feedback loop," *Opt. Express* **18**(13), 13805–13812 (2010).
-

1. Introduction

Free-space beam-steering is important for light detection and ranging (LIDAR), free space communications, and has potential applications for holographic displays and biomedical imaging. LIDAR employs a moving laser beam to sample the environment for optical “echoes” and rapidly collect high resolution three-dimensional images. One can imagine a world where every vehicle employs a LIDAR system for improved safety, for data collection, or to provide feedback for automated driving. This will require advancement beyond the current state of LIDAR technology – which typically costs tens of thousands of dollars and is so large that it has to be mounted on the roof of the vehicle – to LIDAR technology that can be deployed on bumpers or door frames. However, this is only possible with the great reduction in size, weight, cost, and mechanical wear that a fully-integrated solid-state beam-steering chip provides. As integration of photonic elements increases [1], it becomes possible to integrate a phased array beam steering system on a chip, with much higher stability and performance with lower cost than has been previously possible.

Free-space beam steering using silicon photonic chips has been demonstrated using off-chip lasers [2–4], including 2D beam steering in [5] through the use of optical phased arrays and a fiber-coupled input. 2D steering using a two-dimensional phased array has also been demonstrated with an off-chip laser [6], but all of the above required a fiber-coupled input and an off-chip laser, rendering the device impractical as a single-chip beam-steering solution. 1D steering with an on-chip laser – i.e. a truly “steerable laser” – has been demonstrated on the hybrid silicon platform with the laser, amplifiers, phase tuners, and phased array all integrated and fabricated on-chip by Doyle et al. [7–9], but thus far 2D steering using an on-chip laser has not been achieved.

In this paper we present the first fully integrated two-dimensional steerable laser chip on a hybrid III-V/silicon platform which also, to our knowledge, combines the largest number to date of integrated components (164) on a silicon substrate with integrated lasers. This chip includes 2 tunable lasers, 34 amplifiers, and 32 photodiodes utilizing III-V material, as well as 32 phase shifters, 31 MMI couplers and a graded index (GRIN) lens in the silicon-on-insulator (SOI) layer. These combine wavelength tuning with an optical phased array to accomplish 2D beam-steering without the need for moving parts or an external laser.

2. Concept

Beam-steering and shaping can be performed with an optical phased array (OPA) by splitting the output from a laser into an array of phase tuners and emitter elements. The far-field beam shape can be arbitrarily chosen by individually tuning the phase of each channel, however the quality of the beam is subject to limitations due to the finite emitter size and number of emitter elements. In the case of a two-dimensional OPA the number of control elements rapidly scales beyond reasonable numbers for a photonic integrated circuit since in general N^2 steered elements are required for beam-forming in two axes, where N is the number of elements required for beam-forming in a single axis with the desired beam quality [6]. Recently a 1D OPA has demonstrated beam-steering using a single control element by cascading phase-shifters in series [10]. Although this cascaded method could be applied to 2D OPAs it is limited in the second dimension by large pixel size. Additionally, because this method does not control individual phase shifters it is more susceptible to thermal crosstalk such as is common when integrating gain elements on-chip.

A more efficient method of 2D beam-steering can be performed by tuning the wavelength of the light emitted from a surface grating. As the light propagates through the emitter, power scatters off each tooth with a phase delay dependent on the effective index of the mode and the wavelength of light. This effectively becomes a series of closely packed pixels that add up in the far field as a 1D beam. The angle of emission (θ) can be calculated from the grating period (Λ), the waveguide effective index (n_{eff}), and the wavelength (λ) as shown in Eq. (1)

$$\sin \theta = \frac{\Lambda n_{eff} - \lambda}{\Lambda} \quad (1)$$

By combining an OPA with grating emitters and a tunable laser, 2D beam-steering can be achieved with linear scaling of the number of control elements, in fact the number of required elements would be only $N + M$, where N is the number of phase-tuned elements required for high-quality beam-forming in one axis and M is the number of controllable elements in the tunable laser (typically fewer than 4). We use ψ for the steering axis determined by the OPA, and θ for the axis determined by wavelength via the Bragg equation.

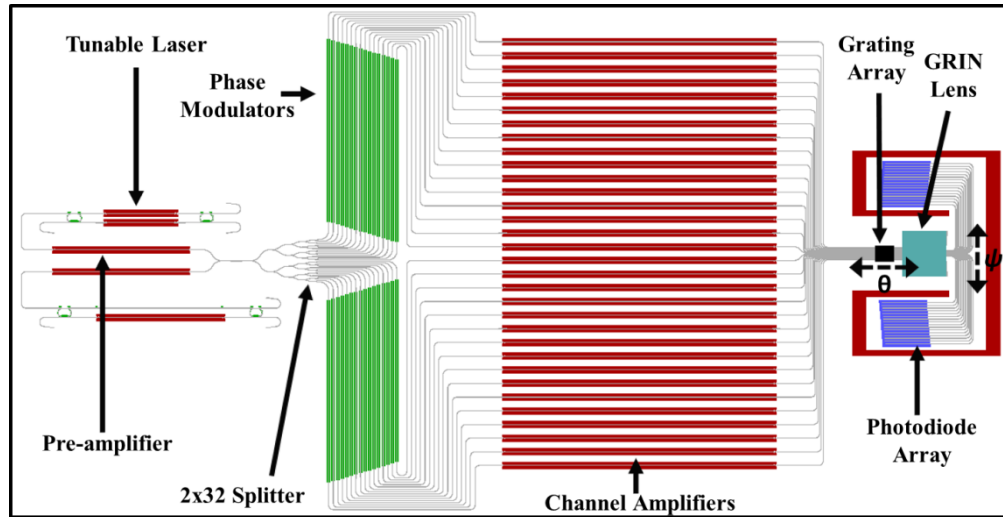


Fig. 1. Layout of the fully integrated PIC. Redundant tunable laser sources are followed by semiconductor optical amplifier (SOA) pre-amplifiers. The signal passes through a 32 channel splitter and is then tuned in both phase and amplitude for each channel. The channels feed a surface grating array where the beam is emitted at an angle determined by wavelength in the θ axis and by relative phase in the ψ axis. A graded index lens images the remaining beam power into the far field and where it is measured by a photodiode array for on-chip feedback.

3. Design

The PIC design begins with two redundant tunable Vernier ring lasers (discussed further below and in Fig. 1). The redundancy can be used to switch between lasers with different tuning ranges to create a much wider wavelength-tuning range overall and thus a wider angular steering range in the θ axis. The laser signal passes through a pre-amplifier prior to being split into 32 channels, each with a phase modulator and an amplifier. For current injection phase tuning, one expects phase-dependent losses, which can be compensated for by the amplifiers to avoid beam distortion. It should be noted that an equal power output from all channels is not ideal for side mode suppression (e.g. as compared with a Gaussian power distribution). Regardless of the desired power distribution, the amplifier array can be used to achieve the desired power distribution with both static adjustments for waveguide and splitter losses and dynamic adjustment for phase tuning induced losses. The optimized beam is emitted from the device via etched waveguide gratings. Any remaining power in the waveguides passes through a graded index (GRIN) lens that images the far field and couples to a photodiode array for on-chip feedback. These elements will now be described in more detail.

3.1 Components

The gain elements for the tunable laser and semiconductor optical amplifier (SOA) are similar to the design reported by Zhang et al. [11] where the mode is shifted upward as it enters a bonded III/V region to partially overlap the pumped quantum wells.

Two laser designs were placed in the PIC and were split between a tested design [12] with 41 nm tuning range and 5.5 mW output power and a new optimized design that is expected to perform similarly but with lower thresholds and higher output powers. Both lasers employ two ring resonators coupled by two bus waveguides with a gain region. The new design omits the gain region from one of the waveguides to reduce losses incurred at the tapered III/V section and replaces it with a thermal phase tuner. The gain region length was also increased from 0.8 to 1.4 mm in the new design to compensate for removing the second gain region. Schematics of the lasers are shown in Fig. 2.

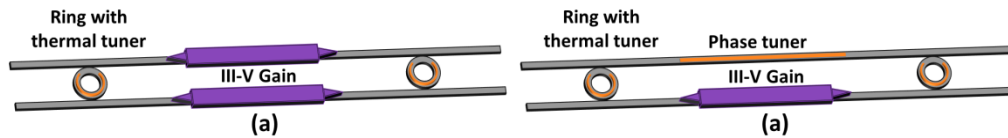


Fig. 2. Schematic of tunable Vernier ring laser with (a) two gain regions and (b) one gain region.

The pre-amplifiers were made 1.5 mm long for amplification of the signal prior to entering the splitter, and the channel amplifiers were made to be 3 mm long to maximize output power from the PIC. It was expected that increasing the length of the pre-amplifier beyond 1.5 mm would not significantly increase the gain due to saturation of the SOA, however the decreased signal following the splitter was expected to see linear gain in the 3 mm amplifiers.

The phase modulators were based on a *p-i-n* silicon diode design [9]. To reduce series resistance, the doped regions were placed 6 μm apart instead of 11, allowing these diodes to move past thermal time constants and rapidly tune using electro-optic phase shifting. This also reduced cross-talk between channels, greatly simplifying the optimization of the output beam.

3.2 Channel output spacing and count

A uniformly spaced OPA generates a main beam as well as undesired side lobes that emit at different angles. These side lobes limit the useful field of view. For a given wavelength, the angular separation between the main lobes and the side lobes is determined by the spacing between emitters as shown in Fig. 3. Thus, decreasing the emitter pitch will increase the useful range of the device until the pitch is limited by waveguide width and mode size.

However, decreasing the total width of the emitter array by decreasing the emitter spacing increases the beam width and reduces the number of resolvable spots. The effect is such that decreasing emitter pitch will keep the number of resolvable spots nearly constant, even though it will increase the field of view, because as the field of view increases so does the size of the spots. A simple way to increase the number of resolvable spots is to keep the emitter pitch small while increasing the array width by increasing the number of channels. However, this adds control complexity since each channel requires individual phase (and possibly amplitude) tuning. Hence 2D steering with a tunable laser and 1D OPA – for which the number of channels scales linearly with array size – becomes much more convenient than a 2D OPA for which the number of channels (and therefore control complexity) scales quadratically with array size.

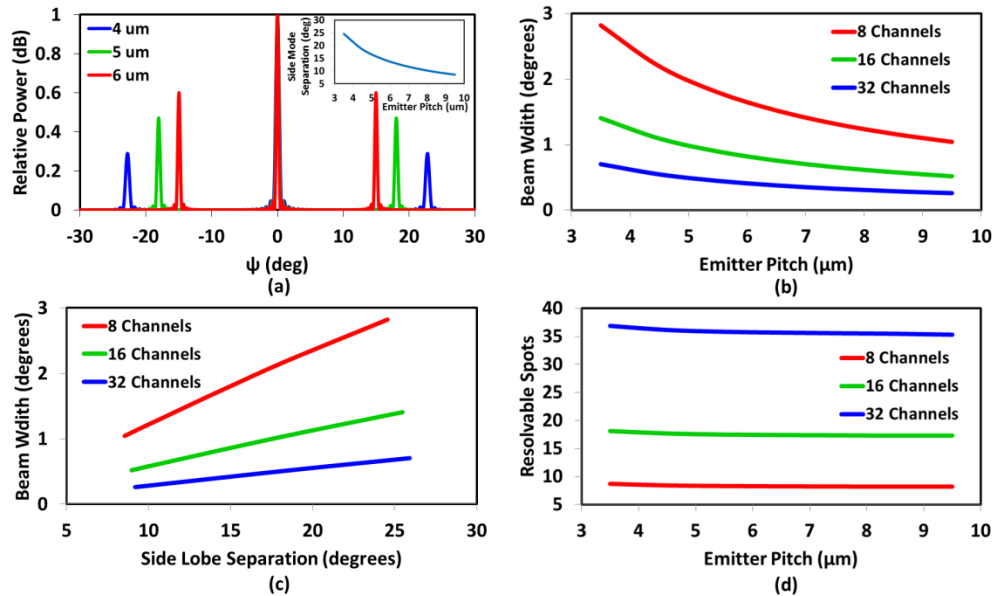


Fig. 3. (a) Calculated angular power distribution for 4, 5, and 6 μm spacing between emitters with an inset of the calculated side mode separation between main lobe peak and side lobe (measured where the side lobe intensity rises to -10 dB relative to main lobe peak which is where the useful field of view ends) vs. emitter pitch, (b) calculated far field beam full width half max (FWHM) vs. emitter pitch for 8, 16, and 32 channels, (c) calculated beam FWHM vs. side lobe separation based on varying emitter pitch, and (d) calculated number of resolvable spots (i.e. side lobe separation divided by beam width) vs. side lobe separation based on varying emitter pitch.

Another approach to increasing side mode suppression is to vary the emitter spacing. For example, using a Gaussian distribution for waveguide pitch results in a very different side mode profile (Fig. 4) with the first major side lobe reduced to the level of the other side lobes. As the chosen angle shifts and the main lobe decreases in intensity the difference becomes even more noticeable. At 0° the uniform array is calculated to contain 53% of the emitted power in the main lobe with a side mode suppression ratio (SMSR) of 5.4 dB, while at 10° it contains only 46% of power with an SMSR of 0.5 dB. The Gaussian array is more uniform across the tuning space with a much better SMSR – the main lobe contains 48% at 0° with an SMSR of 13.9 dB and 45% at 10° with an SMSR of 8.2 dB. However within a field of view that excludes the first major side lobe, the uniform array maintains a higher SMSR over a greater tuning range.

Calculations were made for other configurations, but the uniform and Gaussian array spacing appeared most promising and were selected for fabrication. The uniform array was designed with a 4 μm emitter pitch and 126 μm total width, and the Gaussian array was designed with a 3.4 μm center emitter pitch, 7.1 μm outer emitter pitch, and 144 μm total width. Both arrays used emitters consisting of gratings with a pitch of 550 nm shallowly etched on 2.3 μm wide waveguides. At this pitch the emitters are expected to tune $0.127 \pm 0.02^\circ / \text{nm}$ at wavelengths of 1555 to 1605 nm [13].

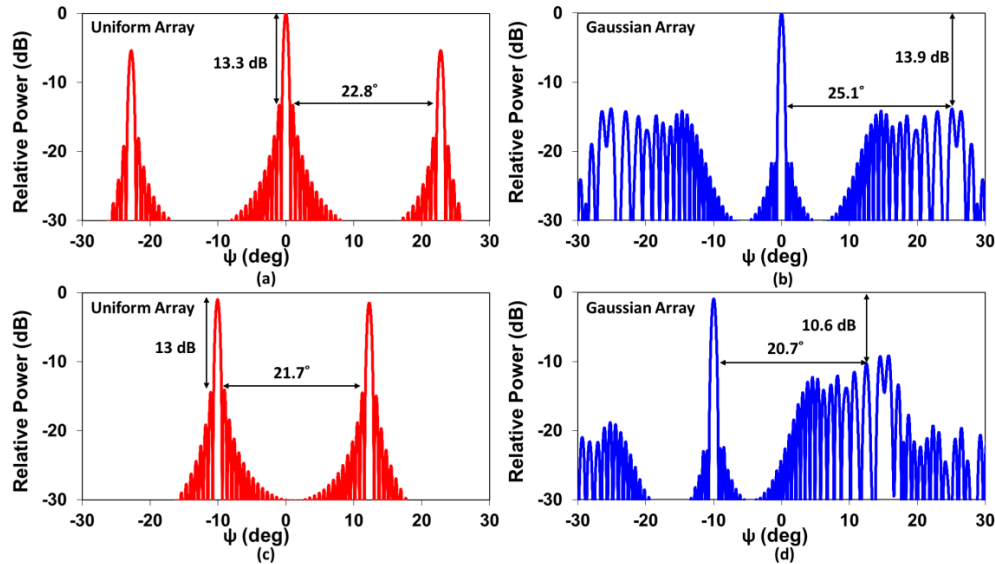


Fig. 4. Calculated far field for (a) uniform and (b) Gaussian emitter spacing using no relative phase or output power differences between channels. Calculated far field for (c) uniform array with linear relative phase shift and (d) Gaussian array with linear relative phase shift adjusted for irregular spacing to tune the main lobe to -10° . The Gaussian array performs better when considering the full signal, but (c)-(d) illustrate the larger tuning range of the uniform array within a field of view while maintaining greater than 10 dB side mode suppression.

3.3 Lens and photodiode array

Most of the optical measurements on this PIC were performed by directly measuring the output beam off-chip using an infrared camera and a lens system as described in Section 5. This technique works well for initial characterization but is insufficient for periodic monitoring, calibration, and control of a field device. Temperature variations can affect the channel amplifier gain, which necessitates a shift in injection current to maintain the proper power distribution. Shifting the injection current also shifts the phase so the phase modulators also require dynamic control. Use of a beam-steering chip requires a feedback mechanism that does not interfere with the output signal and is included on-chip. Such a device has been demonstrated in [16] for power from a 2-channel interferometer, but for the PIC described in this work a means of tracking the interference pattern between all 32 channels was required. To that end, an on-chip measurement system was designed using a 1D graded index lens to image the far field of the ψ axis. The imaged field is placed at the beginning of an array of waveguides that feed a photodiode array to measure the beam angle (Fig. 1).

The lens was fabricated by shallowly etching sub-wavelength holes of varying diameter in an SOI slab that was then covered in PECVD SiO_2 . The hole diameters were selected so as to vary the effective index of the slab parabolically across its width, effectively forming a graded index (GRIN) lens. Figure 5 shows a cross-section of the calculated index profile and the simulated intensity throughout the lens with zero relative phase shift between channels.

The waveguides feeding the photodiode array were placed at the calculated focal length ($473 \mu\text{m}$) with a total width of $64 \mu\text{m}$. There are 32 photodiodes in the array that are expected to span 41° in the far field (the total expected width between the first-order side lobes) with a resolution of 1.3° . This resolution is not high enough to resolve individual spots but is sufficient for coarse recalibration of phase alignment from thermal fluctuations.

A calculation of the beam intensity at the lens focal point is shown in Fig. 6 for several different values of linear phase difference between adjacent channels.

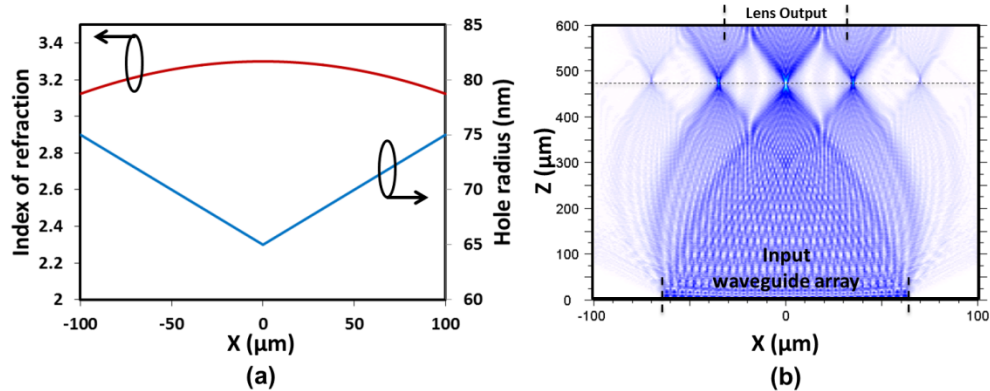


Fig. 5. (a) A cross-section of the calculated refractive index profile for the GRIN lens. The cross section is taken at 250 μm into the lens. (b) Simulated intensity passing through the lens with zero phase shift between channels. The focal length is marked at 473 μm .

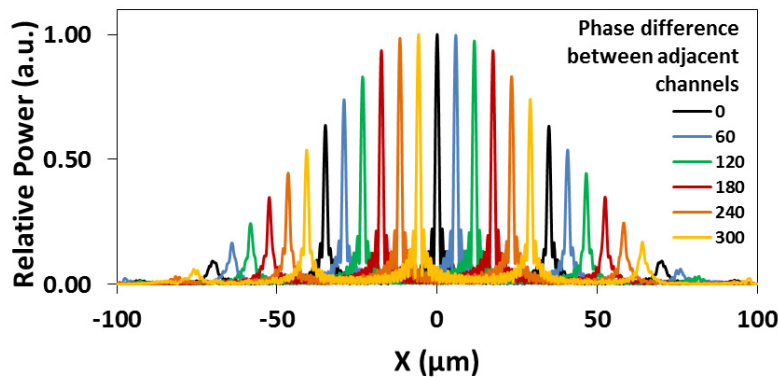


Fig. 6. Calculated lens output power for linear relative phase delays between adjacent channels in degrees.

4. Fabrication

The PIC was fabricated on 500 nm SOI with 1 μm buried oxide. Rib waveguides were patterned using 248 nm DUV lithography and etched 275 nm. *P-i-n* diodes for the phase modulators were made with boron and phosphorus implantation of and a 1050°C anneal. Emitter gratings were then formed over the waveguides by e-beam lithography and etching 50 nm. The gain regions were formed by bonding III-V epitaxial material to the top silicon as per the hybrid silicon process described in [14,15]. The III-V substrate was removed with a mechanical polish and wet-etch. The III-V was then patterned and dry-etched to create gain elements in the laser and amplifier sections but avoid losses in the silicon waveguides. Metal contacts were added through e-beam deposition for gain and phase modulator sections. A buffer layer of SiO_2 was deposited by PECVD. Vias were etched to the contacts and probe metal was deposited.

5. Packaging and test setup

The finished chip was diced and then thinned by mechanically polishing the backside down to 100 μm in order to reduce thermal impedance between the active devices and the heat sink. The backside was metalized for better thermal conduction and then bonded to a gold pad on a BeO carrier using a thin thermally conductive epoxy. The carrier was placed in a copper

mounting block that connected the carrier to a water cooled block with additional epoxy. The signal pads from the chip were wire-bonded to matching pads on the carrier. A pogo-pin adaptor connected the pads on the carrier to a printed circuit board where a series of wires linked the board to the driver and measurement devices. A total of 101 separate signals were required to fully use this chip. Pictures of the finished 6 mm x 11.5 mm chip can be seen in Fig. 7.

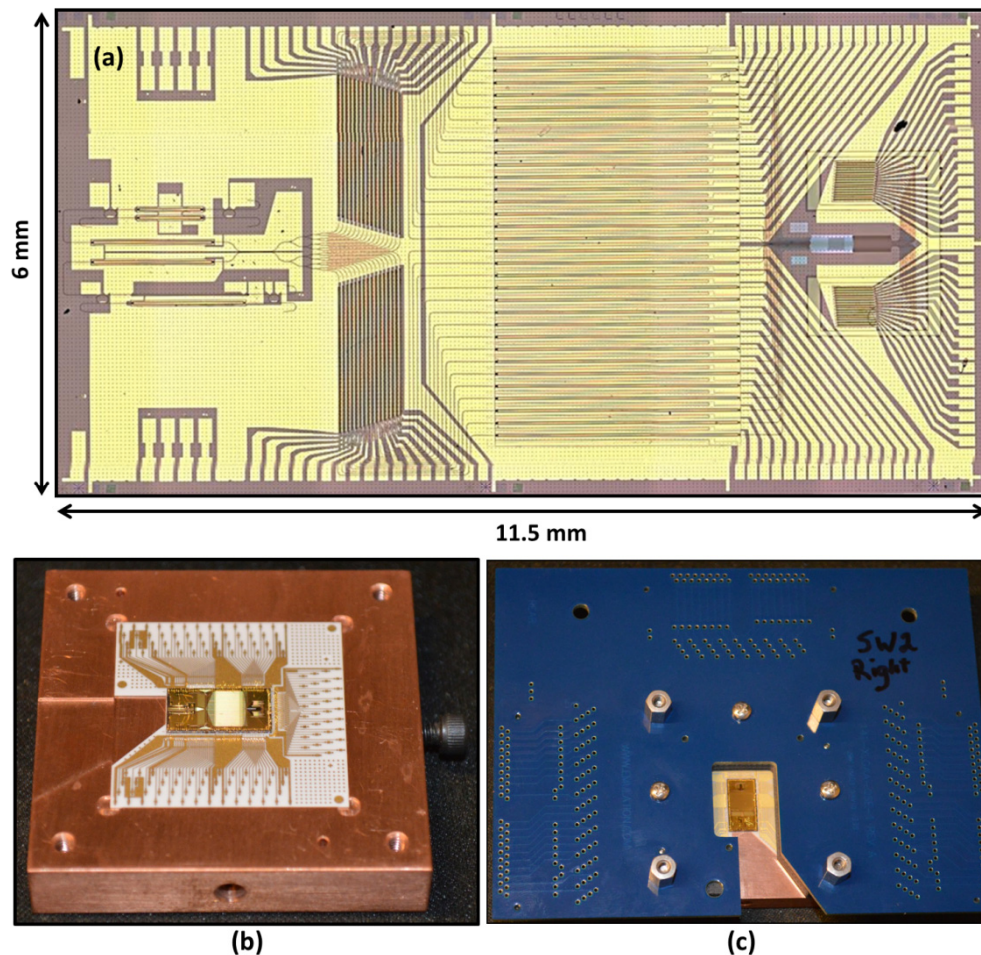


Fig. 7. (a) Confocal microscope picture of the fully integrated beam-steering PIC. The chip size is $y \times z$ cm². (b) Photos of the mounted and wire-bonded chip placed in a water-cooled copper block and (c) the PCB attached to the assembly.

The optical output from the device was measured using two configurations. First, a lens to fiber was placed over the chip to measure the optical spectrum of the device for wavelength characterization. The second configuration is shown in Fig. 8 and used a total of three lenses: Lenses 1 and 3 were used to image the output from the device onto an IR camera and Lens 2, an aspheric lens with high numerical aperture, was used to image the far-field. Lens 2 was placed in a rotating mount to provide easy switching between far- and near-field imaging, as were several neutral density filters to avoid saturating the camera. A polarization controller was also used to align the polarization along the TE axis.

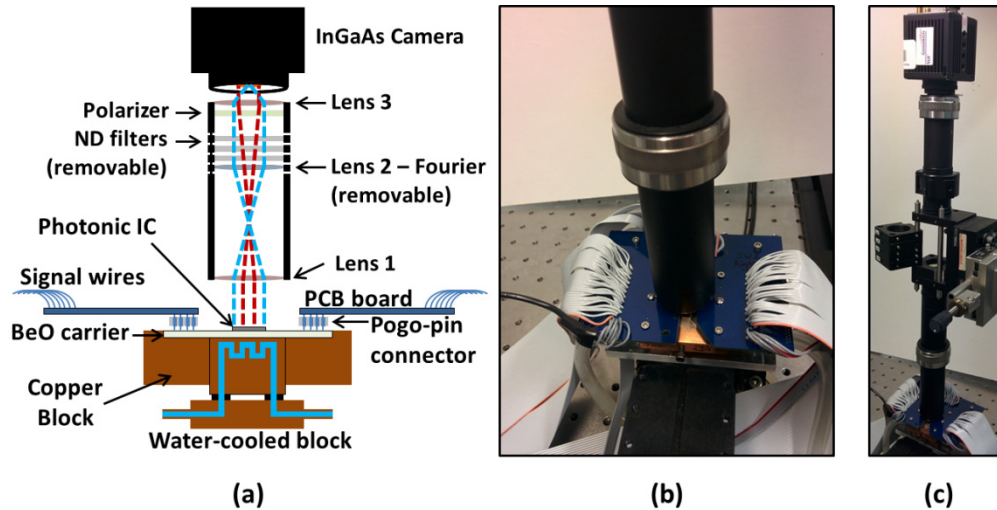


Fig. 8. (a) Schematic of the test setup and (b)-(c) images of the test setup.

6. Results

6.1 Lasers and amplifiers

SEM images of the laser and amplifiers are shown in Fig. 9. Wavelength measurements were performed with a fiber collimator placed over the chip that captured the light after being emitted from the PIC.

The single-gain-section laser performed significantly better than the dual-gain-section lasers (see Fig. 2) with respective threshold currents of 94 and 168mA. The SOAs also exhibited lasing at currents between 200 and 400 mA due to small reflections off of the tapers.

To characterize wavelength tuning the laser gain was pumped at 260 mA, the pre-amplifier was pumped at 180 mA, and the rest of the chip was un-pumped. Scattered light from the laser and pre-amplifier was collected using the fiber collimator for direct measurement. The laser exhibited tuning over 34.5 nm (Fig. 10). Additional testing with the lens setup showed good correlation of measured and expected angle tuning (based on wavelength measurements), thus verifying that the grating couplers are working as designed. Wavelength tuning efficiency of 0.28 nm/mW was achieved from the laser that gives a predicted angle tuning efficiency of 0.030 °/mW. The measured angle tuning efficiency was 0.034 °/mW. The beam was steered a total of 4.4° in θ with a tuning efficiency of 0.127°/nm as designed and predicted in Section 3.2.

The yield on working gain elements was 93% leaving 3 channels with un-pumped amplifiers.

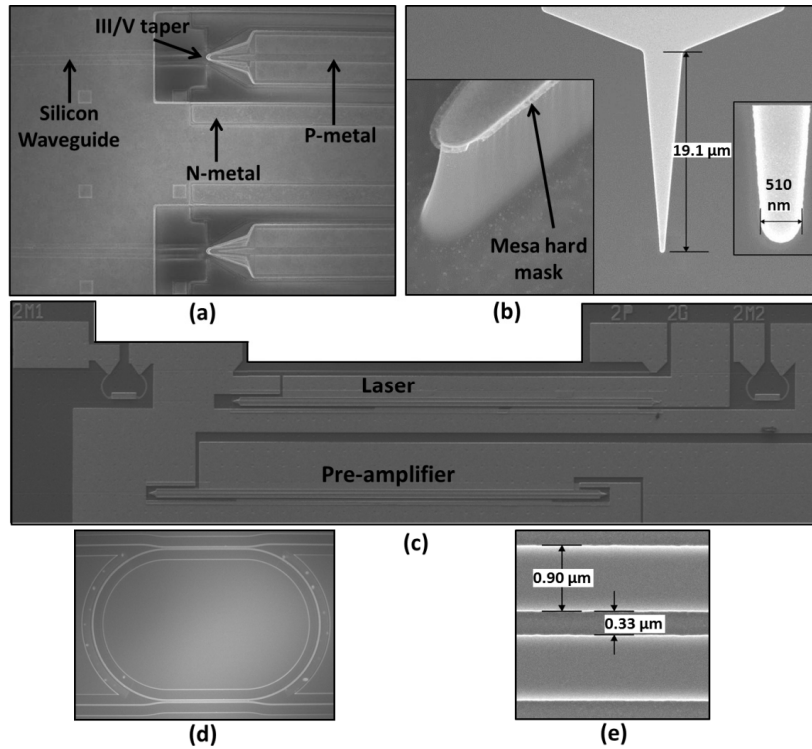


Fig. 9. SEMs of (a) laser and pre-amplifier gain elements, (b) InP tapers for adiabatic transitions between III/V gain and silicon waveguides with magnified images of the taper tip immediately following mesa etching, (c) completed laser and pre-amplifier, (d) ring mirror and (e) ring-to-bus coupler.

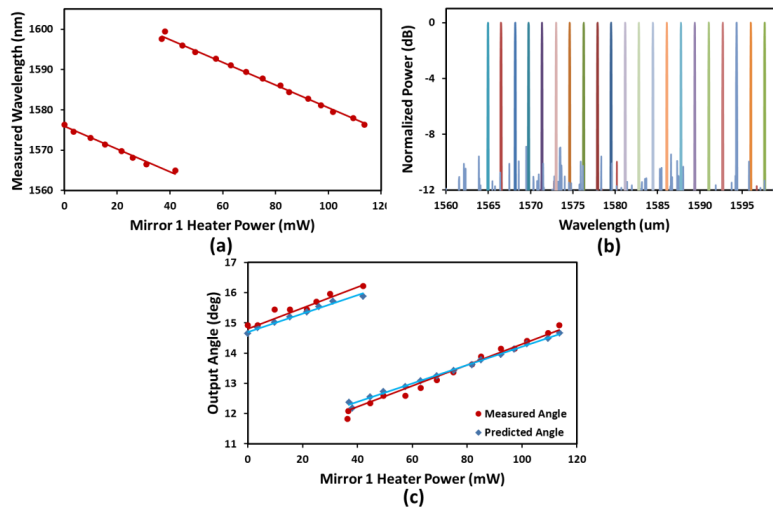


Fig. 10. (a) Measured peak wavelength vs. tuning power from one mirror, (b) measured optical spectra, and (c) measured output angle vs. predicted output angle (from wavelength measurement). A wavelength tuning efficiency of 0.28 nm/mW was achieved and the tuning efficiency of predicted and measured angle were 0.030 and 0.034 °/mW respectively. Since the laser was integrated on-chip it was unable to be measured individually so the full spectra SMSR is not available.

6.2 Phase modulators

The phase modulators were characterized using Mach-Zehnder test structures. Although designed to work electro-optically they worked almost entirely in the thermo-optic (TO) regime as evidenced by a clear dependence on power rather than a dependence on current (Fig. 11). When electro-optic (EO) tuning is present, phase tuning typically begins in a current-dependent regime that gives way to a power-dependent regime as thermal effects dominate. In silicon, TO and EO tuning shift the index of refraction in opposing directions (TO causes positive change with increasing injected electrical power while EO causes negative index change with increasing injected electrical current) so the crossover between the two is easily discerned. In the case of this chip the thermal tuning was almost immediately dominant and a tuning efficiency of $160 \text{ mW}/\pi$ was measured.

The thermo-optic dominance is attributed to a high resistance in the silicon layer from process contamination. Test runs of the modulators without III/V bonding showed EO tuning with efficiencies of $14 \text{ mA}/\pi$ (a low power regime where TO tuning is minimal) and a 3dB bandwidth greater than 50 MHz. It is believed that damage to the contacts, as well as possible damage to the trench region around the rib, is the cause of the discrepancy between the test devices and the phase modulators on the full PIC – i.e. increased resistance in the current path led to increased joule heating. A comparison of transmission line measurements (TLMs) between the two processing runs shows that the sheet resistance on the integrated phase modulators was greater than 7 times that of the devices processed without III/V. The integrated modulators exhibited a 3 dB bandwidth greater than 300 kHz.

The phase-modulator yield was 97% on the beam-steering PIC.

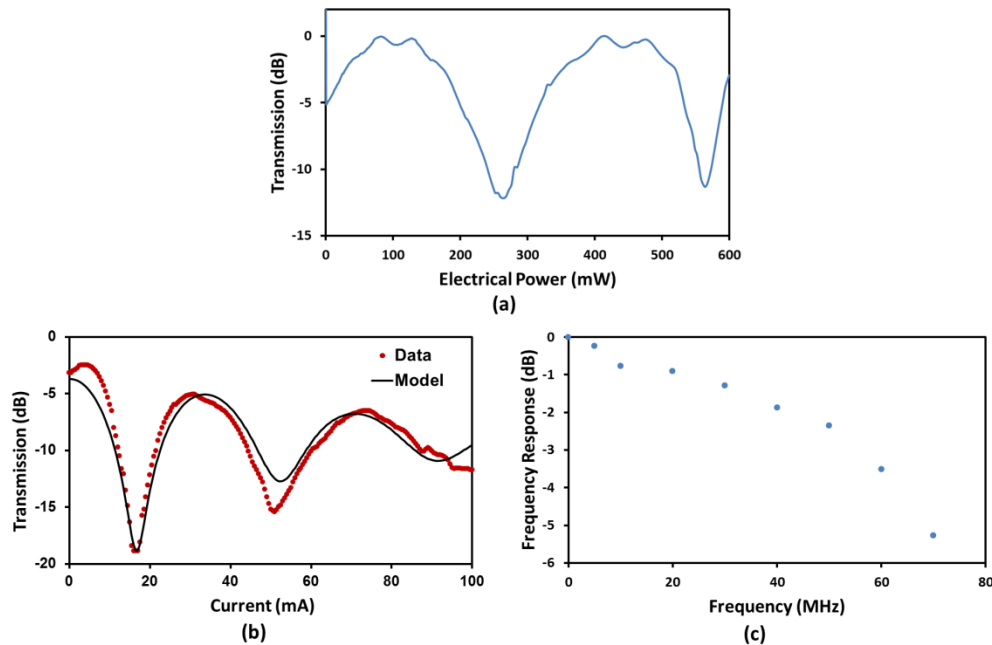


Fig. 11. (a) Transmission through a 2 mm Mach-Zehnder test structure showing a phase modulator dependency on power implying a thermo-optically dominated device on the integrated chip. Test run measurements of similar devices showing (b) $14 \text{ mA}/\pi$ tuning efficiency with data and modeled fit and (c) a 3dB bandwidth greater than 50 MHz.

6.3 Lens and photodiode array

SEM images of the lens and output gratings are shown in Fig. 13, and a larger image of the lens and photodiode array is shown in Fig. 14. Unfortunately, errors in the proximity correction of the e-beam lithography meant that attempts to characterize the beam angle using the lens and photodiode array were unsuccessful as the photo-current produced in each photodiode was not well correlated with the angle.

Characterization of the lens and photodiode array was done by pumping one of the central channel amplifiers at high enough current to induce lasing from taper reflections and then measuring the reverse photocurrent in the photodiode array. Test photodiodes were also measured with an external laser to determine the responsivity and quantum efficiency (Fig. 12). For the wavelengths available in the PIC, the quantum efficiency averaged 45% and the responsivity averaged 0.57 A/W for 470 μm long photodiodes. 100% yield on the photodiodes was achieved.

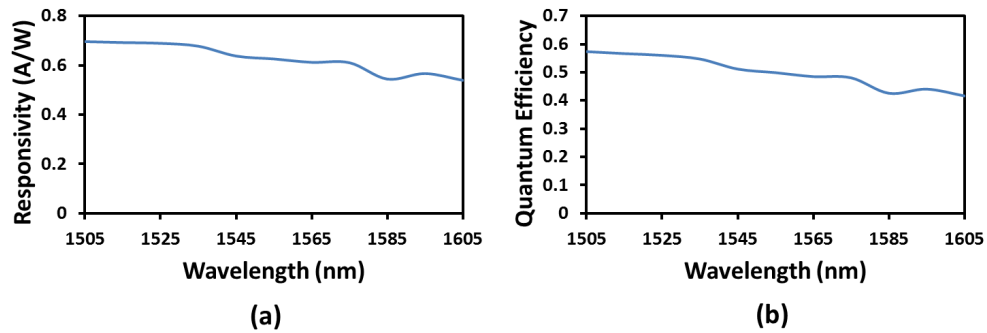


Fig. 12. (a) Responsivity and (b) quantum efficiency of the 470 μm long photodiodes at -5 V.

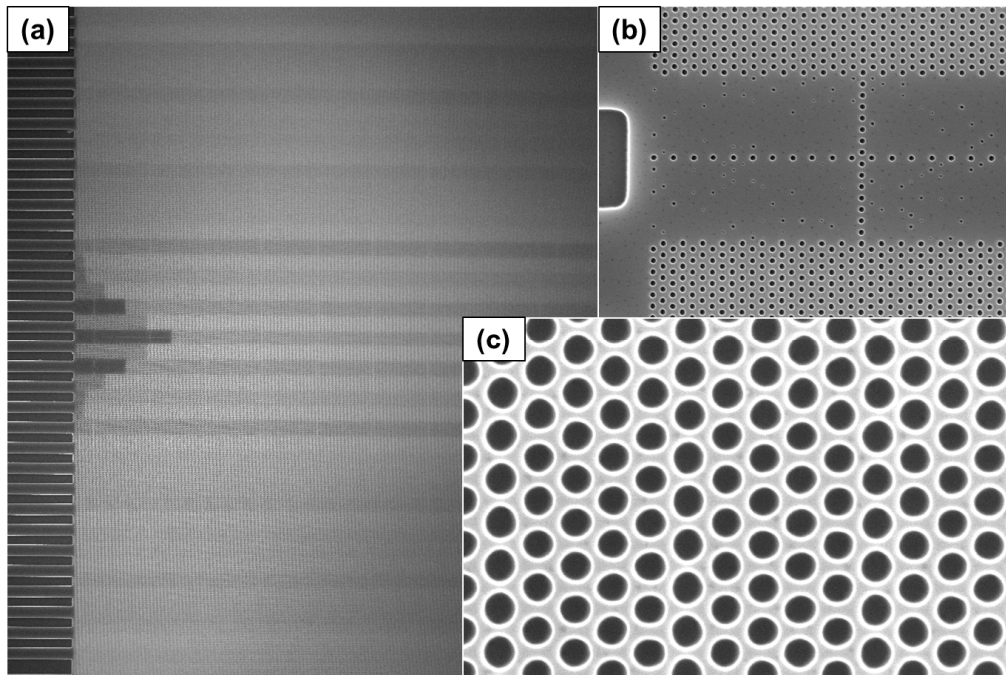


Fig. 13. SEMs of (a) input waveguides and the beginning of the GRIN lens, (b) a zoomed in SEM of insufficiently etched holes that led to lens distortion of the beam, and (c) a close-up image of the photonic crystal lens etched spots.

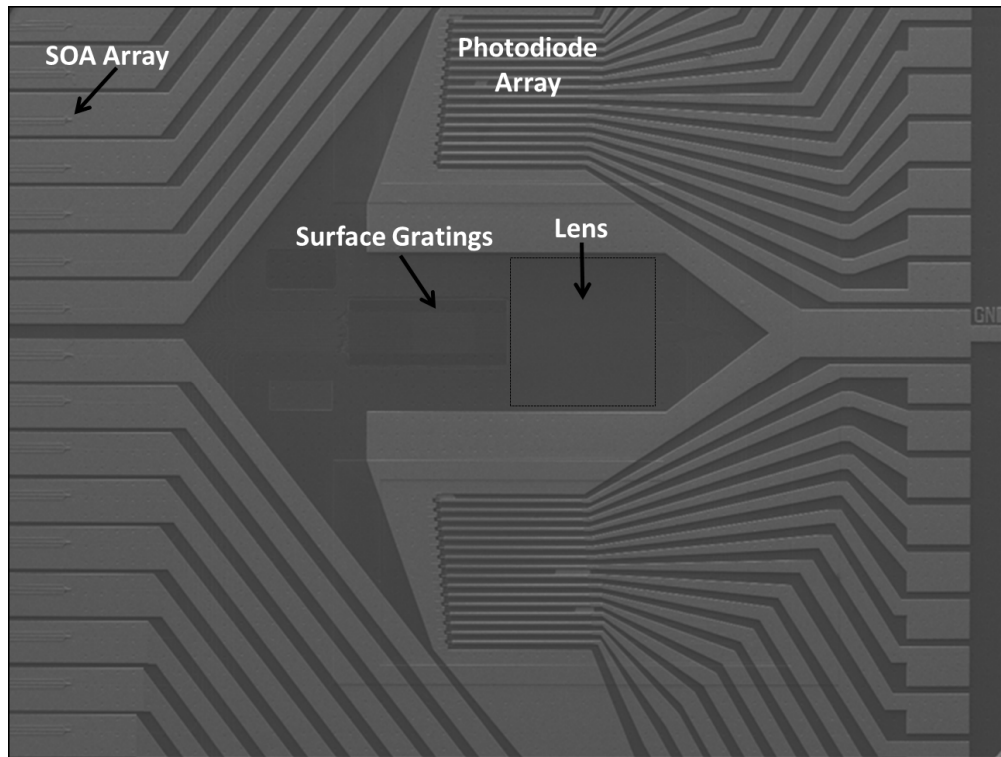


Fig. 14. SEM of output grating array, lens and photodiode array.

6.4 Integrated 32 channel device

For two-dimensional beam-steering the laser gain current was set to 260 mA and the pre-amplifier gain current was set to 240 mA. After tuning the laser's mirror and phase heaters to select the desired wavelength, the phase modulator and channel amplifier currents were optimized by use of a hill-climbing algorithm as described in [5]. The beam optimization is measured as the power at the desired angle divided by the maximum power of the side lobes within a window of angles. For a given phase modulator channel the beam optimization is measured for several current shifts around the last value where the shift is a multiple (-2, -1, 0, 1, 2) of some delta. The delta is chosen by taking a fit of the beam optimization at each current, calculating a slope, and shifting the current for that channel in the direction of improved beam optimization. More intricate algorithms were attempted, but it was found that the simple hill-climbing algorithm was best able to optimize the beam. Beam-steering of 23° (ψ) x 3.6° (θ) was achieved (Fig. 15) with respective beam widths of 1° x 0.6° and greater than 70% background suppression. This corresponds to 23 x 6 (a total of 138) resolvable spots. The side lobe suppression was limited to 70% by a combination of inconsistent gain characteristics across the amplifier array, multimode output from some channels, and 3 failed channel amplifiers.

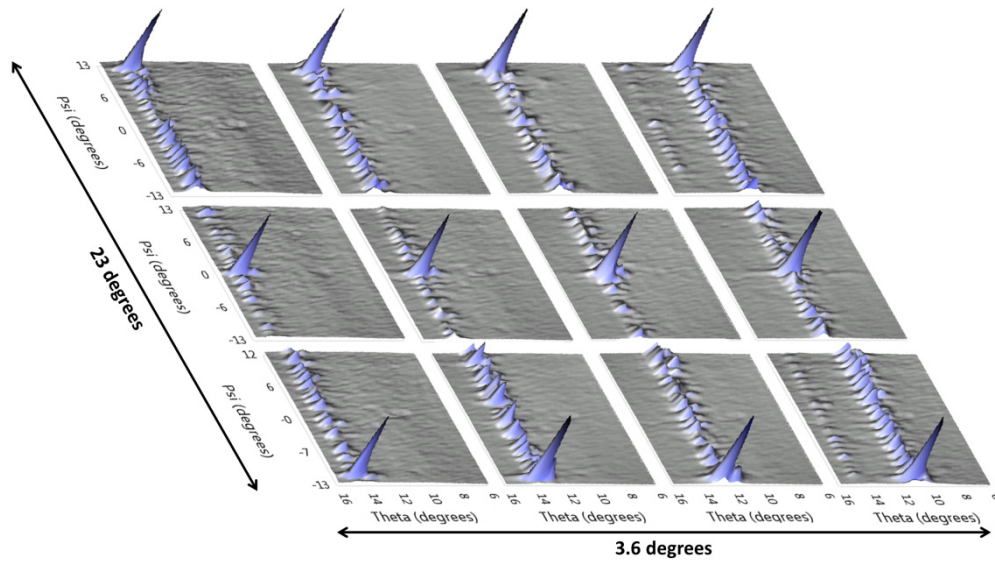


Fig. 15. Two-dimensional beam-steering plots spanning 23° in ψ and 3.6° in θ .

7. Conclusion

We have presented the first fully-integrated free-space beam-steering chip on the hybrid-silicon platform. The PIC incorporates a total of 164 components with 9 different component types. Steering over $23^\circ \times 3.6^\circ$ was exhibited with beam widths of $1^\circ \times 0.6^\circ$ giving a total of 138 resolvable spots in the far field with 5.5 dB background suppression.

Acknowledgments

This work was supported by DARPA MTO in the SWEEPER program, grant #HR0011-10-2-0003. The authors thank Josh Conway and Milan Masanovic for useful discussions.